ACS OMEGA

http://pubs.acs.org/journal/acsodf

Article

Preparation and Characterization of Physically Activated Carbon and Its Energetic Application for All-Solid-State Supercapacitors: A Case Study

Aziz Ahmad, Mohammed Ashraf Gondal,* Muhammad Hassan, Rashid Iqbal, Sami Ullah, Atif Saeed Alzahrani, Waqar Ali Memon, Fazal Mabood, and Saad Melhi

Cite This: *ACS Omega* 2023, 8, 21653−21663

Read Online

ACCESS | Metrics & More | Article Recommendations | Supporting Information

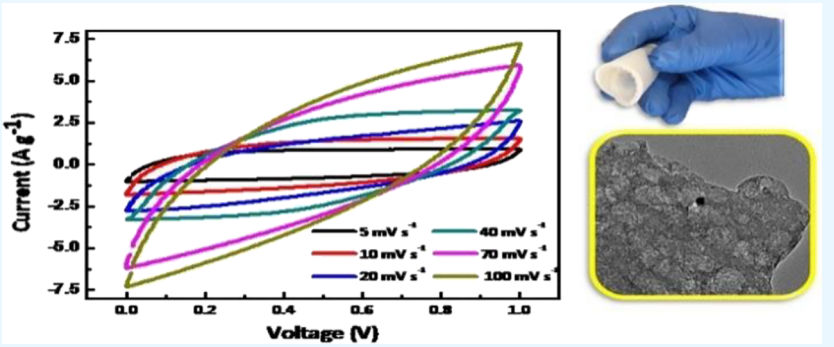

ABSTRACT: Biomass-derived activated carbons have gained significant attention as electrode materials for supercapacitors (SCs) due to their renewability, low-cost, and ready availability. In this work, we have derived physically activated carbon from date seed biomass as symmetric electrodes and PVA/KOH has been used as a gel polymer electrolyte for all-solid-state SCs. Initially, the date seed biomass was carbonized at 600 °C (C-600) and then it was used to obtain physically activated carbon through CO_2 activation at 850 °C (C-850). The SEM and TEM images of C-850 displayed its porous, flaky, and multilayer type morphologies. The fabricated electrodes from C-850 with PVA/KOH electrolytes showed the best electrochemical performances in SCs (Lu et al. *Energy Environ. Sci.*, **2014**, *7*, 2160) application. Cyclic voltammetry was performed from 5 to 100 mV s^{-1}, illustrating an electric double layer behavior. The C-850 electrode delivered a specific capacitance of 138.12 F g^{-1} at 5 mV s^{-1}, whereas it retained 16 F g^{-1} capacitance at 100 mV s^{-1}. Our assembled all-solid-state SCs exhibit an energy density of 9.6 Wh kg^{-1} with a power density of 87.86 W kg^{-1}. The internal and charge transfer resistances of the assembled SCs were 0.54 and 17.86 Ω, respectively. These innovative findings provide a universal and KOH-free activation process for the synthesis of physically activated carbon for all solid-state SCs applications.

1. INTRODUCTION

The global climate anomalies and cumulative depletion of nonrenewable energy sources have encouraged the fast growth of sustainable energy sources, pushing forward a crucial need for smart and productive devices for energy storage.[1−7] The two biggest and commonly used electrochemical devices for energy storage are supercapacitors and batteries. Supercapacitors (SCs) differ from batteries because of their fast charging, high power density, and discharging rate capabilities. These features make SCs suitable for use in applications where one requires a high power uptake.[8−10] Electrochemical capacitors are generally composed of electrolytes, separators, and electrodes. Electrodes are responsible for charge storage, while electrolytes and separators assist in ion migration between electrodes and keep them separated from each other. In the past decades, SCs have achieved remarkable consideration due to their long lifespan and high power density.[11] Application of SCs includes use in rechargeable pulsed power sources particularly, in hybrid power forms in electric vehicles, and in complementary power sources in different applications due to their remarkable cyclic stability and high power density.[11−16]

SCs are mainly divided into two types, viz., redox and electrical double layer capacitors (EDLCs). Redox SCs store charges through fast reversible Faradic reactions on the

Received: February 16, 2023
Accepted: June 1, 2023
Published: June 9, 2023

Scheme 1. Schematic Illustration of Physically Activated Carbon Prepared from Date Biomass

electrolyte/electrode interface. They exhibit larger capacitance than EDLCs owing to the additional charge migration between the applied potentials.[8,17,18] However, the cyclic stability of redox SCs is not too much prolonged because the electrode candidates deteriorate due to the fast Faradic reactions.[8] Active materials such as NiO_x,[19] $RuO_2{\cdot}xH_2O$,[20] CoO_x,[21,22] poly(anthraquinonyl)sulfide,[23] conducting polymers, *e.g.*, polythiophene, and polyaniline[24−28] have been used as redox-active materials in redox supercapacitors.[11] In contrast, EDLCs store electrolyte ions/charges on the surfaces of the used electrode materials, *e.g.*, activated carbon due to the electrostatic attraction among the adsorbed electrolyte ions and polarized electrode surfaces, resulting in two charged layers called Helmholtz double layers.[8,29,30] For the EDLC formation, the electrode materials must hold high enough conductivity and specific surface area. EDLCs are mainly assembled from activated carbon because of their high surface area, controllable porosity, nontoxicity, and good enough electrical conductivity.[12,13,16,31]

Carbon and carbon-based electrodes have gained widespread applications in various energy storage systems because they are low-cost and own thermochemical stability, processability, structural tenability, and textural characteristics to achieve the necessities of the particular applications. The design of the hierarchical porous materials creates larger effective specific[2] surface areas, which attains the fast ion transportation.[32−34] In the past two decades, biomass-based ACs have attained tremendous consideration due to their abundant feedstocks, low cost, and porosity[3] and they promote added value to bio-waste.[35,36] Several bio-wastes such as tea leaf residues,[37,4] nutshells,[38,39] vegetable wastes,[40,41] coconut shells,[42,43] and apricot shells[44] have been employed as precursor materials to obtain activated carbon (AC). Moreover, the presence of various organic functional groups provide thermal stability to their skeleton, which make them more promising.[45] The methods involved in the production of AC can be divided mainly into chemical activation, physical activation, and physical−chemical activation. Among these, the process for the physically activated carbon preparation is advantageous due to its cost-effectiveness and environmental friendliness.[46−48] Moreover, the mechanism of this approach involves the occurrence of redox reactions among the carbon component of carbon materials and various oxidizing gases including $CO_{2(g)}$, $O_{2(g)}$, $H_2O_{(g)}$, and their mixtures.[3,49,50] Among them, activation with $CO_{2(g)}$ and $H_2O_{(g)}$ is more manageable because the endothermic reactions could reduce the excessive burn-off, which not only enhances the AC yield but also participates in the controllable formation of porous structures.[51] By contrast, the chemical activation method mainly uses NaOH, KOH, H_3PO_4, $NaHCO_3$, and $ZnCl_2$. However, this method is expensive and associated with environmental issues.[3]

Electrolytes play a significant role in SCs, whereas their stability, potential range, and ionic conductivity might affect the electrochemical performance.[52] These SCs, which comprised liquid electrolytes, suffer from self-discharge, current leakage, explosion, corrosion, and bulky shape, as in the same case of liquid electrolytes in batteries.[11,53,54] Thus, significant attention has been given to assemble all solid-state SCs using solid−gel polymer electrolytes because they have high packaging flexibility, easy handling without leaking toxic liquids, advantageous mechanical properties, high ionic conductivity, appropriate electrolyte−electrode contact, and the capability to make thin films of desirable area where required.[11,55,56] Some of the recently reported polymer/gel electrolytes in SCs application are PMMA-EC-PC-$LiClO_4$,[57,58] glycerol/KOH,[55] PVA/H_2SO_4,[59] PVA/H_3PO_4,[60] and PVA/KOH.[8] This paper presents the synthesis of a gel polymer electrolyte from polyvinyl alcohol and potassium hydroxide (PVA/KOH) and physically activated carbon (PAC) derived from date biomass. An all-solid-state SCs was configured utilizing PVA/KOH as the solid electrolyte as well as the separator and PAC as the electrode material. The electrochemical performance of the configured SCs was evaluated via cyclic voltammetry, Bode plot, impedance spectroscopy, and galvanic charge−discharge tests. The specific capacitance of the C-850 electrode and energy density of SCs were 138.12 F g^{-1} and 9.6 Wh kg^{-1}at a power density of 87.86 W kg^{-1}, respectively, whereas the charge transfer resistance was 17.86 Ω calculated through the Nyquist plot.

2. EXPERIMENTAL SECTION

2.1. Used Chemicals. All the chemicals used were of analytical rank and were utilized as received. Potassium hydroxide (KOH), polyvinyl alcohol $[C_2H_4O]_x$, ethanol (C_2H_5OH), and acetone (C_2H_6O) were ordered from Sigma-Aldrich. Polyvinylidene fluoride (PVDF, $-(C_2H_2F_2)_n-$), carbon black (CB), and *N*-methyl-2-pyrrolidone (NMP, C_5H_9NO) were ordered from MTI Corp. Deionized water was used for the solution preparation.

2.2. Preparation of Samples. Date seeds were amassed from a local date seed packing company. The date seeds were washed repeatedly by tap and distilled water. The cleaned seeds were then ground into a fine powder and was used as raw materials. In the next step, the obtained date powder was kept in a furnace for carbonization at 873 K (600 °C) and it was kept for 1 h under the N_2 environment. The obtained carbonized carbon was named C-600. To get a refined surface with small size particles, C-600 was ground further into small particles using a mortar and pestle. Further, the ground C-600 was kept in the furnace and activated by CO_2 at 1123 K (850 °C) for 60 min. The achieved physically activated carbon was washed with distilled water and ethanol. The final obtained physically activated carbon was named as C-850 and were tested as an electrode candidate for the all-solid-state SCs with

https://doi.org/10.1021/acsomega.3c01065
ACS Omega 2023, 8, 21653−21663

Scheme 2. PVA/KOH Thick Paste, Thin Film Formation, and Its Flexible Nature

no further chemical treatment. The schematic illustration for the synthesis of C-600 and C-850 is shown in Scheme 1.

2.3. Sample Characterization. The surface morphologies of the achieved C-600 and C-850 were characterized using a field emission scanning electron microscope (FESEM, HITACHI SU8220) and transmission electron microscope (TEM 200 KV, Tecnai G20 STWIN). Elemental analysis of the used materials was performed by X-ray photoelectron spectroscopy (XPS, ESCALAB 250Xi XPS Microprobe, microfocusing X-ray monochromator, Thermo Scientific, USA). The amorphous nature of C-600 and C-850 was analyzed by X-ray diffraction (XRD, MiniFlex, Rigaku). The diffractometer was used at 10 mA current, 30 kV voltage, and 0.15416 nm λ. The Raman spectra of C-600 and C-850 were measured at room temperature by Raman spectroscopy (iHR320 image spectrometer equipped with a CCD detector, HORIBA). A Micromeritics ASAP 2020 machine was utilized to analyze the pore size distribution and specific surface area (SSA) by Brunauer–Emmett–Teller (BET) N_2 adsorption/desorption. The thermal stabilities of the C-600 and C-850 were tested by thermogravimetric analysis (TGA). A Pyris Diamond TGA/DTA equipment (Perkin Elmer Instruments CO. Ltd., USA) was used. TGA results of the aforementioned samples were recorded between 30 and 1000 °C with a heating speed of 5 °C min^{-1} under a N_2 environment. The Fourier transform infrared (FT-IR) spectra of C-600 and C-850 were obtained through KBr disks in transmission mode using a Perkin-Elmer Spectrum-One Spectrometer.

2.4. Synthesis of the PVA/KOH Electrolyte. A gel polymer electrolyte of PVA/KOH was prepared by the method reported in the literature.[61] Initially, 2 g of PVA was added to 40 mL of distilled water. A temperature around 95 °C was fixed, and the PVA/H_2O mixture was stirred until the PVA dissolved completely and a transparent solution appeared. At this stage, an equal amount of the dissolved KOH (2 g in 20 mL of H_2O) was added dropwise to the transparent PVA solution. The PVA/KOH mixture was stirred until the water evaporated (95 °C) and a thick paste was achieved. The PVA/KOH transparent paste was added into a glass Petri dish, which was kept at room temperature for 3 days to form a wet gel thin film. The prepared PVA/KOH gel electrolyte thin film with flexibility is shown in Scheme 2.

2.5. Assembling of the All-Solid-State SCs. The electrodes were fabricated from C-850 (70%), carbon black (CB, 20%), and -polyvinylidene fluoride (PVDF, 5%). A fixed proportion of C-850, CB, and PVDF was mixed and ground well using a mortar and pestle. The weight of active materials in the electrodes was 2.2 mg. In the next step, the ground mixture and 5 mL of *N*-methyl-2-pyrrolidone (NMP) were placed in a beaker and stirred vigorously at 85 °C for 5 h to form a thick homogeneous paste. The gained homogeneous thick paste was casted on Al foil using a doctor blade and vacuum-dried at 80 °C overnight. The casted electrodes on the Al foil was cut into small slices, and an all-solid-state symmetric SCs was configured. The configuration of Swagelok assembled SCs was kept as Al/C-850//PVA-KOH//C-850/Al to perform the electrochemical tests.

2.6. Electrochemical Tests. The electrochemical tests of the assembled solid-state SCs were performed using a potentiostat (PGSTAT302N, Metrohm Autolab) at ambient temperature. Galvanostatic charge–discharge (GCD), electrochemical impedance spectroscopy (EIS), Bode plot, and cyclic voltammetry (CV) were applied to investigate the charge transfer resistance, electric double formation, and the activated carbon nature of the fabricated electrodes. The specific capacitance from CV and charge–discharge curves were calculated using eq 1 and eq 2, whereas the energy and power densities were calculated using eq 3 and 4 as follows:[55,62]

$$C_s = \frac{1}{m \times v \times \Delta V} \int_{V1}^{V2} I \, dV (\mathrm{F\ g^{-1}}) \tag{1}$$

$$C_s = \frac{I \times \Delta t}{m \times \Delta V} (\mathrm{F\ g^{-1}}) \tag{2}$$

$$E_d = \frac{1/2 \times C_s}{3.6} \Delta V^2 (\mathrm{Wh\ kg^{-1}}) \tag{3}$$

$$P_d = \frac{E_d}{\Delta t} \times 3600 (\mathrm{W\ kg^{-1}}) \tag{4}$$

where C_s represents the specific capacitance in Farad per gram (F g^{-1}), m stands for the active mass of electrode in g, $\int_{V1}^{V2} I \, dV$ represents the area below the CV curve, ΔV is the difference in applied potential, v is the applied scan speed (V s^{-1}), I is the applied current in ampere, and Δt is the difference in discharge time in s. E_d and P_d are the energy and power densities of the assembled all-solid Al/C-850//PVA-KOH//C-850/Al symmetric SCs and are measured in Wh kg^{-1} and W kg^{-1}, respectively.

3. RESULTS AND DISCUSSION

To eliminate the bulk of volatile compounds (lignin, cellulose, hemicellulose, and lignocellulose)[45] and achieve a carbon material with enhanced porosity, date biomass was first exposed to a pretreatment at 600 °C under an inert environment followed by the activation with CO_2. The carbon obtained at 600 °C under an inert environment of N_2 is due to the removal of soft volatile matter. As this carbon was prepared at 600 °C, so it was named C-600. During the physical activation process at high temperatures, at first, oxygen species of the activating agent interact with the tarry off-product restricted in the pores, and thus this process leads toward the opening of the closed pores. The development of heteropores occurred as the oxidizing agent burnt the areas that are more reactive in the carbon skeleton of C-600 at high temperatures. In this study, as we used CO_2 as the activating agent at 850 °C, the obtained physically activated carbon was named C-850.

https://doi.org/10.1021/acsomega.3c01065
ACS Omega 2023, 8, 21653–21663

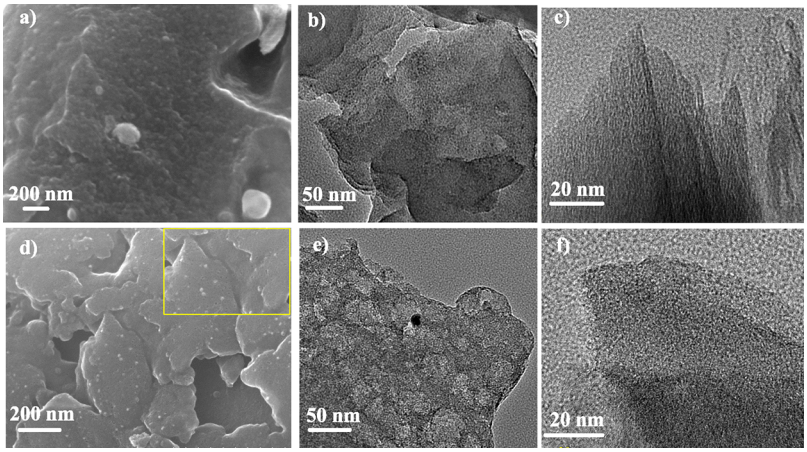

Figure 1. (a) SEM image of C-600, (b, c) HRTEM images of C-600, (d) SEM image of C-850, and (e, f) HRTEM images of C-850.

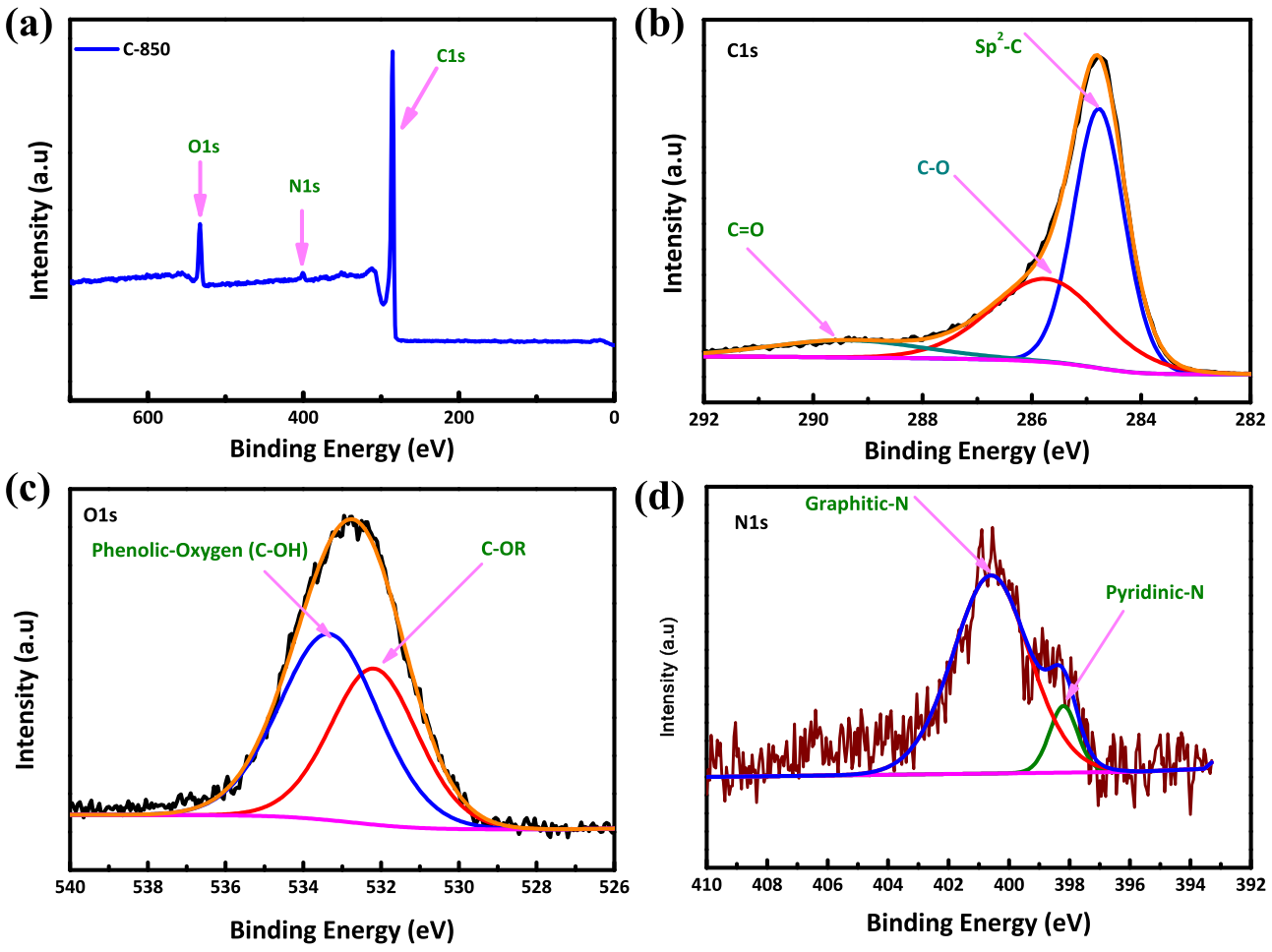

Figure 2. Typical XPS surface chemical analysis. (a) Average survey scan and corresponding high-resolution spectra of (b) C 1s, (c) O 1s, and (d) N 1s of the C-850 activated carbon.

SEM, EDS, and HRTEM were used to study the surface morphology, elemental composition, and multilayer nature of C-600 and C-850. Figure 1a–c shows the SEM images of C-600 at various magnifications. Figure 1a illustrates that C-600 exhibited a foam-type morphology with no obvious pore formation, whereas the HRTEM images (Figure 1b,c) of C-600 at high and low magnifications illustrate its flat-type and multilayer nature morphology. Figure 1d exhibits the SEM image of C-850 with apparent pore formation. A particular area in Figure 1d, enclosed by a yellow rectangle, was magnified further, which illustrated the apparent heteropore formation with a sheet-type morphology. The HRTEM images (Figure 1e,f) of C-850 further confirmed the apparent pore formation, sheet-type morphology, and its amorphous nature. The chemical composition on the surfaces of C-600 and C-850 was confirmed by XPS analysis, as shown in Figure S1 and Figure 2. The typical XPS spectra of both the samples show the presence of carbon (C 1s), oxygen (O 1s), and nitrogen (N

https://doi.org/10.1021/acsomega.3c01065
ACS Omega 2023, 8, 21653−21663

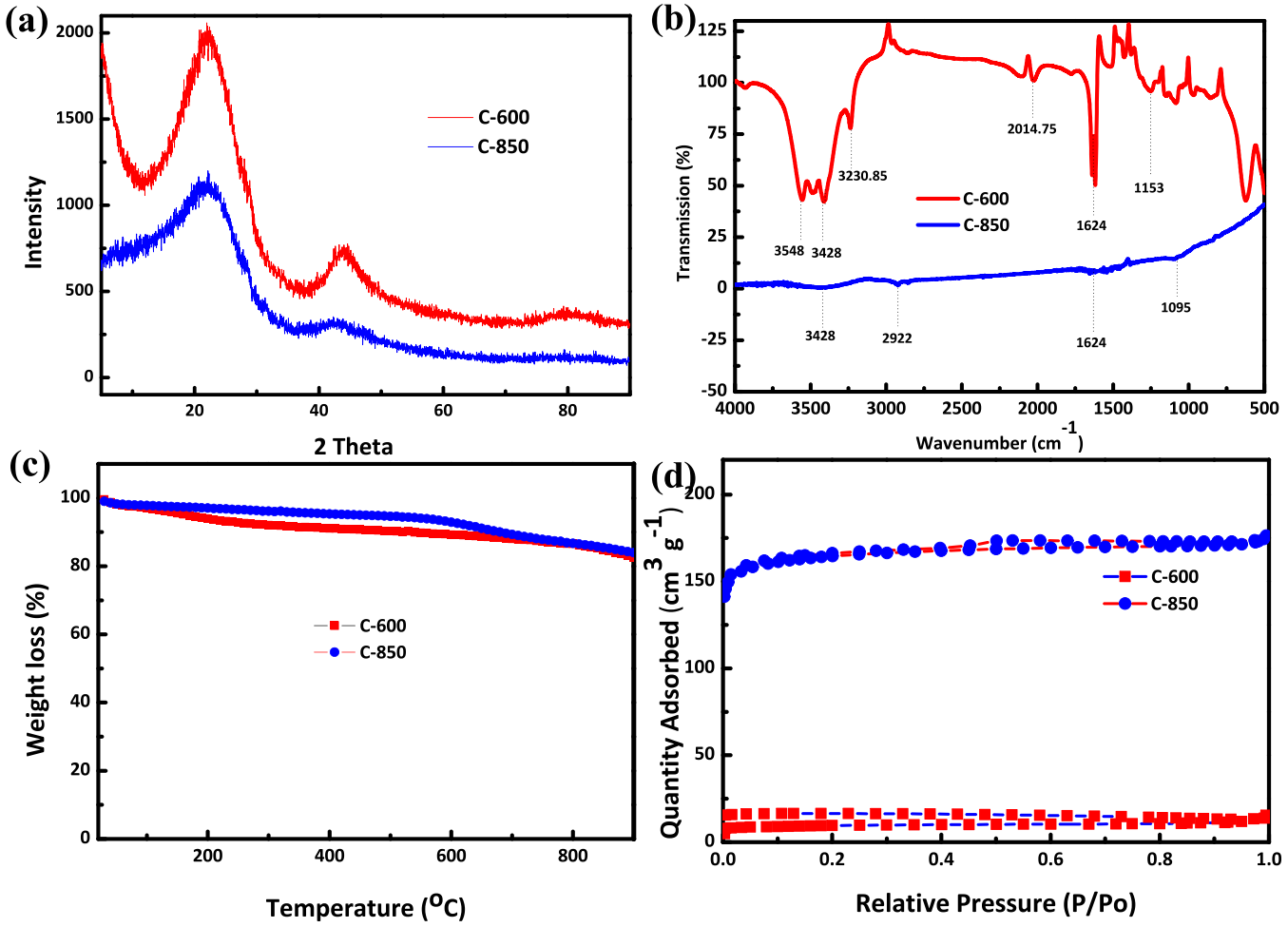

Figure 3. (a) XRD, (b) FT-IR, (c) TGA, and (d) BET characterization of C-600 and C-850 samples.

1s) as the main constituent elements (Figure S1b and Figure 2b). The high-resolution deconvoluted spectrum of C 1s indicates three peaks at 289, 285.6, and 284.7 eV, which are assigned to the carbon−oxygen double bond (C═O), carbon−oxygen single bond (C−O), and sp^2 hybridized carbon, respectively.(Figure S1b and Figure 2b).[63,64] The peaks at 289 and 285.6 eV confirm the presence of oxygen that are in the form of carboxylic (COOH) and ether (C-OR) functional groups. Figure S1c and Figure 2c illustrate the deconvoluted spectra of O 1s at 533.43 and 532.2 eV, showing another indication of the oxygen availability in C-600 and C-850 samples. The peak component at 533.43 eV is assigned to the oxygen single bonded to the aromatic carbon (phenolic oxygen as C-OH), while the component peak at 532.2 eV is ascribed to the carbon−oxygen ether-like single bond (C-OR).[65] The high-resolution deconvoluted peaks of N 1s are shown in Figure S1d and Figure 2d. The deconvoluted peaks of N 1s at 401 and 398.2 eV show the presence of two nitrogen types available in the C-600 and C-850 samples, *i.e.*, the graphitic nitrogen and pyridinic nitrogen.[63]

The XRD measurements of the produced samples were performed to reveal their structures, whether they exhibit crystalline or amorphous nature. Both the physically and chemically activated carbons illustrate a diffraction peak (002) around $2\theta = 23°$ and overlapped peak (100 and 101) around $2\theta = 44°$.[66] It was observed that before and after the CO_2 activation process, the obtained C-600 and C-850 showed a well introduced graphitic stacking signal at $2\theta = 22.25°$ and a broad weak signal at $2\theta = 43.59°$. The peaks that appeared in C-850 with high intensity might be owing to the formation of high-degree interlayer condensation and improved conductivity.[66,67] The peaks at $2\theta = 22.25°$ and $2\theta = 43.59°$ are indexed to the (002) and (100) planes of the graphitic carbon, which are typically amorphous structures (Figure 3a).[68]

FT-IR spectroscopy provides significant information regarding the chemical nature of the materials. Figure 3b shows the comparative FTIR spectra of C-600 and C-850. The FT-IR spectrum of C-600 indicates that it consists of various functional groups that mainly come from various compounds present in the biomass. In C-600, the peaks around 3548 cm^{-1} are attributed to the O−H functional group in phenol, whereas the peaks around 3428, 3230.85, 2031.16, 1624, 2014.75, and 1153 cm^{-1} are attributed to the O−H stretching vibration, C≡C stretching vibration with a weak band, strong conjugated peak of C═C, aromatic ring, and stretching vibration of C−O functional groups. The remaining peaks, which are smaller than 1000 cm^{-1}, can be attributed to the fingerprint region.[69] In contrast, the FT-IR spectrum of C-850 illustrated that some of the functional groups along with their corresponding peaks on 3548, 3230.85, 2031.16, and 1153 cm^{-1} disappeared or attenuated after activation with CO_2 at high temperatures. Further, the spectrum of C-850 showed new peaks at 2922 and 1095 cm^{-1}, which indicated the presence of methylene (−CH_2−) and C−O stretching

https://doi.org/10.1021/acsomega.3c01065
ACS Omega 2023, 8, 21653−21663

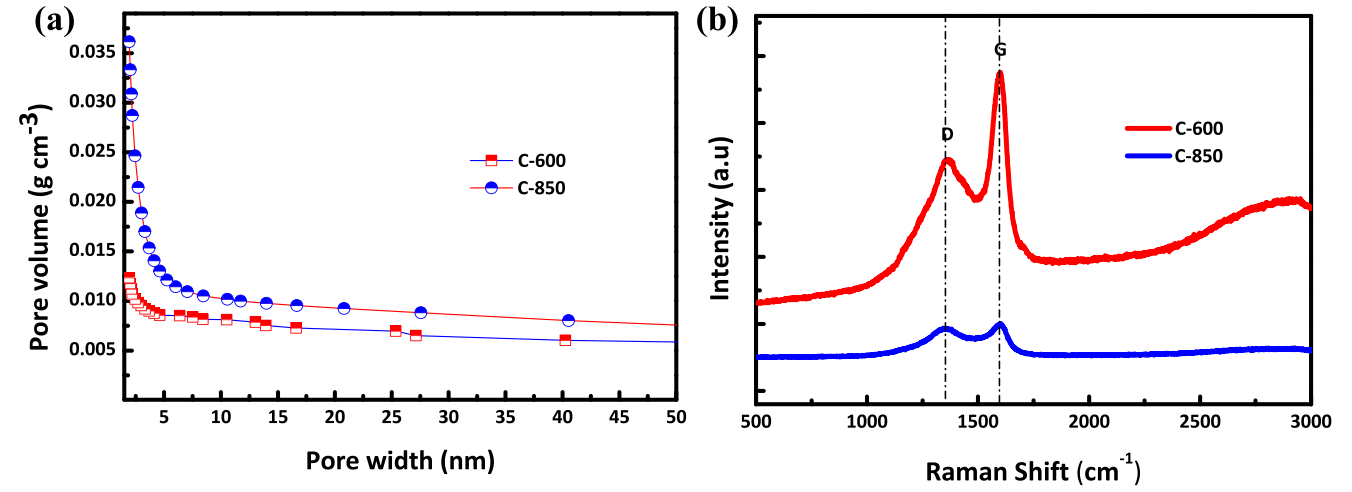

Figure 4. (a) BJH pore size distribution and (b) Raman spectra of the C-600 and C-850 samples.

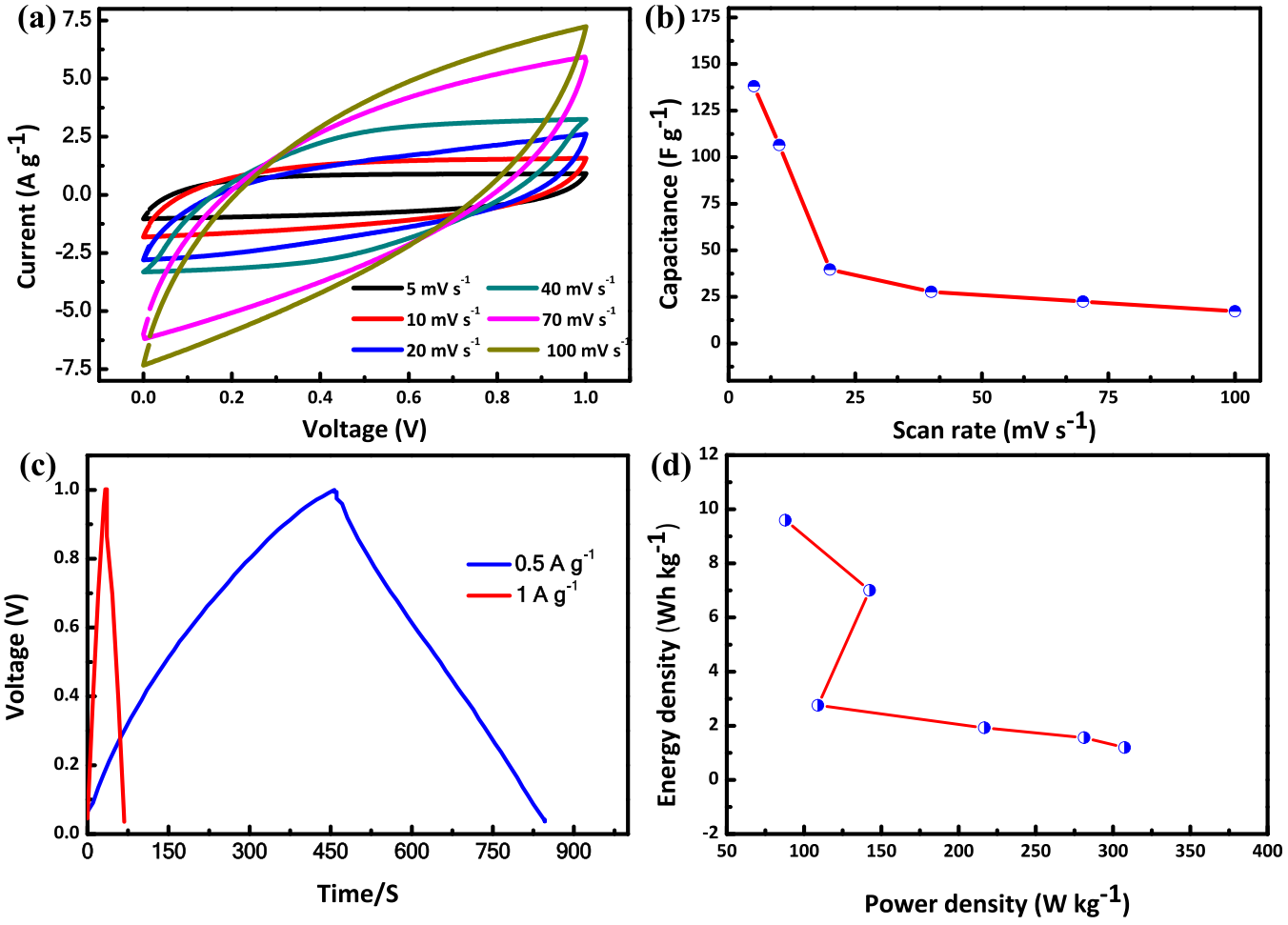

Figure 5. Electrochemical measurements of the C-850 electrode with the PVA/KOH gel polymer electrolyte: (a) CV curves at various scan rates, (b) specific capacitance of a single electrode at different current densities, (c) galvanostatic charge−discharge curves with various current densities, and (d) Ragone plot of coin cell SCs.

vibrations, respectively. Thus, a clear difference was seen among the two samples before and after the activation process. TGA is a valuable tool that is used to distinguish the difference between the stabilities of C-600 and C-850. Figure 3c depicts the TGA curves of both the samples. The TGA analysis of both the samples was conducted in the temperature range from 20 to 900 °C. The TGA curve of C-600 showed a gradual weight loss with an overall retention of 77% of the initial weight. By contrast, the TGA line of C-850 shows a gradual weight loss and its weight retention after 900 °C was up to 82% of the initial weight. The excellent thermal stability of C-850 might be due to the further degradation of the available

https://doi.org/10.1021/acsomega.3c01065
ACS Omega 2023, 8, 21653−21663

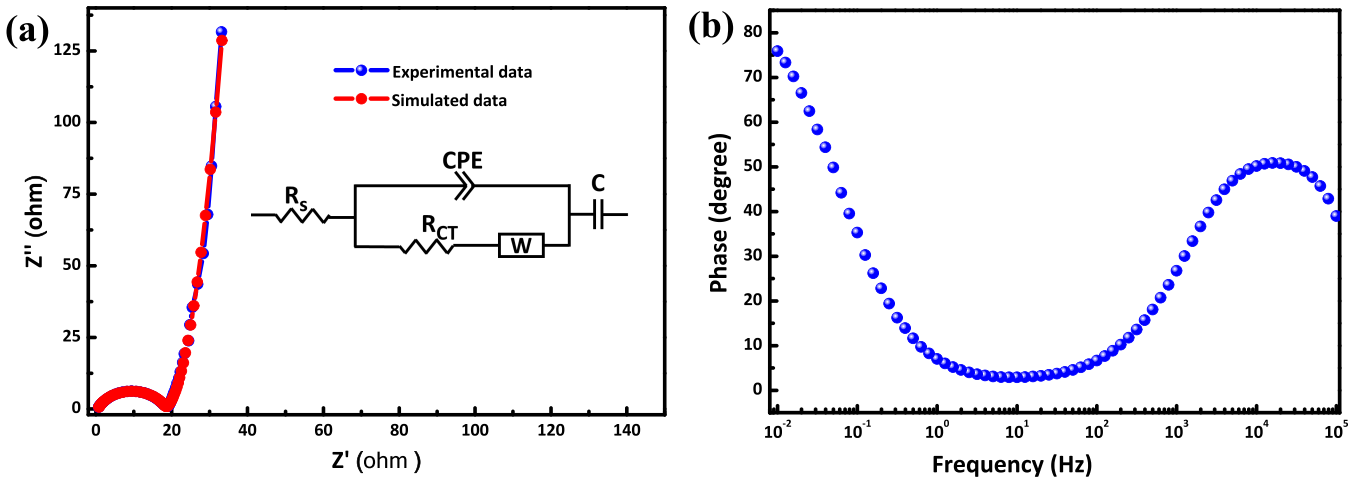

Figure 6. (a) Nyquist plots of the experimental and simulated data for the C-850 electrode with the inset of the equivalent circuit and (b) phase angle values *vs* frequency graph.

compounds into carbon at high temperatures, illustrating the stability of physically activated carbon. The N_2 adsorption and desorption isotherms of C-600 and C-850 samples are presented in Figure 3d. The isotherms for C-600 followed a type I curve, whereas the physically activated carbon (C-850) followed type IV isotherms. A small hysteresis loop is observed for sample C-850 from P/P_o = 0.44 to P/P_o = 0.804, which is because of the mesopore formation. In other words, the isotherm of C-850 indicates the mesoporous adsorption occurrence on its surface. These results indicate the mesopore and heteropore formation after activating C-600 with CO_2 at high temperatures. The reason for the formation of more mesopores is the burning off of the majority of the micropores as a result of high temperature activation.[70,71] The BET surface areas of C-600 and C-850 were found to be 35.21 and 659.56 $m^2\ g^{-1}$, respectively. The BET of C-850 is higher than that of C-600, showing the effective activation by carbon dioxide, which has significantly improved the pore formation during the activation process at high temperatures.

The pore size distributions of C-600 and C-850 were calculated through Barrett−Joyner−Halenda Model (BJH), as presented in Figure 4a. It was observed that both the samples exhibited a heteroporous structure (mixture of micro-, meso-, and heteropores). The characteristic micro- and mesopore diameters were found in the range of 1.8−2.9 nm, respectively. Raman spectroscopy was performed to determine the graphitic and defective nature of the samples. In the Raman spectra, both the C-600 and C-850 showed two peaks located at 1358 and 1596 cm^{-1}, which were assigned to the D and G bands, respectively (Figure 4b). The D-band corresponds to the double-resonance Raman process in disordered carbons,[72] while the G-band is associated with the graphite structure.[73] In other words, the G-band is related to the sp^2 vibration in the C−C planar graphite and the D-band showed the disordered structure.[68] The intensity of the D-band depends on the defects and disordered structure in the carbon skeleton. The low intensity peak ratio between the D- and G-bands (I_D/I_G = 0.733) shows the more graphitic and less defective nature of C-600 and C-850.

We have explained the abovementioned discoveries of C-600 and C-850 samples. Though C-600 is amorphous and show graphitic properties, due to its low BET (35.21 $m^2\ g^{-1}$), it was not suitable to test its electrochemical performance for SCs application. This is because this surface area is not that much favorable to form an electric double layer for all-solid-state capacitors. Therefore, for further electrochemical measurements, only C-850 was used due to its appropriate specific surface area. The electrochemical measurement of the assembled symmetric SCs, configured as Al/C-850//PVA-KOH//C-850/Al in a Swagelok cell, was performed. Figure 5a depicts the CV curves of C-850 electrodes at different scan rates from 5 to 100 mV s^{-1} with an operation potential window between 0 and 1 V. The CV curves depict nearly rectangular forms at each scan rate. At a low scan rate of 5 mV s^{-1}, the C-850 electrodes show a CV with symmetrical rectangular shape without the appearance of any obvious Faradaic peaks, which is the characteristic of EDLCs. At scan rates of 5, 10, and 20 mV s^{-1}, the fabricated electrodes retained their rectangular shape with no gradual distortion. However, a gradual distortion has been observed at scan rates of 40, 70, and 100 mV s^{-1}, which is due to the fast ion migration between the electrodes and electrolyte ions. The specific capacitance of the C-850 electrode was determined from the CV scan rates using eq 1. The influence of the scan speeds on the specific capacitance (C_s) of the C-850 electrode was also calculated, as given by Figure 5b. A specific capacitance of 138.12 F g^{-1} was achieved at a scan speed of 5 mV s^{-1}. It can be seen in Figure 5b that with the increase in scan speed (5 to 100 mV s^{-1}), the area below the curves was increased, and as a result, the corresponding specific capacitance was decreased from 138.12 to 17.21 F g^{-1}. The specific capacitance values of the C-850 electrode at 10, 20, 40, 70, and 100 mV s^{-1} were calculated as 106.56, 40, 28, 22.5, and 17.21, respectively (Figure 5b). The increasing trend of specific capacitance at low scan speeds was observed because at slow scan speed, the electrolyte ions were absorbed entirely into the pores of electrodes. Therefore, it is expected that the entire active electrode surface was used for the storage of electrolyte ions. By contrast, at high scan speeds, the ions do not have time long enough to transport completely into the electrode materials' pores, and thus, only the external active surface is used for ion storage.[8,74] The specific surface area (SSA) is a critical parameter to achieve the high SCs performance; however, it is not mandatory to gain high specific capacitance always with larger SSA. Though the SSA of the C-850 electrode is not that much excellent when compared to other activated carbons, it

https://doi.org/10.1021/acsomega.3c01065
ACS Omega 2023, 8, 21653−21663

still shows a specific capacitance of 138.12 F g^{-1}. Some electrode materials achieved high capacitance even with a smaller SSA because in their case, the total available pores are utilized by the ions.[8,75] Moreover, some of the activated carbons hold a large SSA but own small pore sizes (micropores) and offer less electrochemical performance when compared with the activated carbon possessing smaller SSA but with a larger pore shape such as the meso- and macropores along with the micropores.[55] The galvanostatic charge−discharge (GCD) test was conducted for the C-850-based all-solid-state SCs. Figure 5c shows the symmetric and triangle shape at different current rates, which illustrated the phenomenon of electric double layer formation. At a current density of 0.5 A g^{-1}, a specific capacitance of 88.4 F g^{-1} was calculated from the GCD using eq 2. An energy density of 9.6 Wh kg^{-1} at a power density of 87.86 W kg^{-1} was achieved for the assembled SCs, as shown in Figure 5d. The electrodes retained an energy density of 1.2 Wh kg^{-1} when the power density achieved to 307.46 W kg^{-1}. Both the energy and power densities were calculated using eq 3 and eq 4, respectively.

A NaOH-activated carbon electrode prepared from date palm fronds showed a specific capacitance up to 156.8 F g^{-1} at 0.4 A g^{-1}.[76] A similar value of 150 F g^{-1} at 0.3 A g^{-1} was reported by Farma et al. using KOH-CO_2-activated carbon from empty fruit bunches of oil palm.[77] In another study, a commercial activated carbon was treated and added to waste palm and activated with KOH that exhibited 226.0 F g^{-1} at 0.5 A g^{-1} using a PVA-based gel electrolyte.[78] A CO_2-activated carbon electrode derived from date palm fronds at the same current density of 1 A g^{-1} achieved 56.8 F g^{-1}.[76] The electrodes assembled from our prepared physically activated carbon showed a specific capacitance of 88.4 F g^{-1} at 0.5 A g^{-1}, demonstrating the significant contribution of this work to the research community. A detailed comparison of various activated carbons and their supercapacitors is shown in Table S1. To further understand the ion transportation and electrode resistance, EIS and the corresponding Nyquist plot were obtained in the frequency range from 100 kHz to 10 mHz (Figure 6a). The Nyquist plot is composed of the real and imaginary parts of the impedance that assist in calculating the different resistances (R) related to the device. The low frequency region in the Nyquist plot displays a sharp growing curve, revealing the capacitive nature of the assembled device. A slope in the low frequency region or the inclined line above the semicircle shoulder in the low frequency region is termed as the Warburg impedance (W), which is associated to the ion diffusion into porous channels of electrodes.[55,79,80] In the high frequency region, the x-intersection illustrates the ohmic resistance of the electrolyte and the internal resistance of the electrode, which is defined as R_S. The semicircle from the high to medium frequency region corresponds to the charge transfer resistance (R_{CT}).[80] The EIS data were simulated through the inset model in Figure 6a, and the values obtained for the R_S and R_{CT} were 0.54 and 17.86 Ω, respectively. These results revealed the low resistance in an all-solid-state SCs. The obtained Nyquist plot data was simulated through the inset model. In Figure 6a, the experimental and simulated data obtained for the C-850-based all-solid-state SCs are presented by the blue and red lines, respectively. The values calculated for the R_S and R_{CT} are based on the simulated data of the Nyquist plot. In the applied model, CPE reflected the interparticle electronic resistance of the electrodes.[81] Further, the data developed by the EIS analysis was utilized to draw the Bode plot from the phase angle value on the y-axis and the frequency on the x-axis (Figure 6b). The Bode plot curve indicated the wide trend in the high frequency region that increased nearly vertically in the low frequency region. At the low frequency region, the phase angle value was measured to be 76.6°, which showed the capacitive behavior of the assembled SCs, and this capacitive behavior is almost similar to the capacitive behavior of the ideal SCs, *i.e.*, 90°.[62,82]

We have further gone through the literature survey and used the Ohm's law to calculate the equivalent series resistance (R_{ESR})[83] from the charge−discharge curves at 0.5 and 1 A g^{-1} using eq 5

$$R = \frac{\Delta V}{I} \tag{5}$$

Similarly, the R_{ESR} value can also be calculated from the galvanostatic charge−discharge measurements at different current densities (50 Ω at 0.5 A g^{-1} and 135 Ω at 1 A g^{-1}). The R_{ESR} value obtained from EIS measurement is usually estimated from the width of the semicircle on the x-axis, which is around 18 Ω in our case. Ideally, the R_{ESR} obtained at different current densities should be the same. In the case of supercapacitors, high resistance might be created due to the fast ion transport during the charge large current passage through the device. This is the main reason that the potential drop in GCD curves increases as the current drawn from it is increased. Moreover, this discussion has been added and highlighted in the revised manuscript.

4. CONCLUSIONS

In summary, a universal and chemical activating agent-free strategy was employed to prepare C-850 activated carbon at 850 °C from C-600 by using CO_2 as the activating agent. The samples reported in this paper were characterized by SEM, HRTEM, XRD, EDX, TGA, BET, FT-IR, and Raman techniques. The SEM and HRTEM images revealed that C-600 exhibited a flat and multilayer-type morphology with a very low SSA, while the physically activated C-850 displayed a flat, multilayer, and porous structure having an SSA of 659.56 m^2 g^{-1}. The XRD and Raman characterization of C-850 showed its graphitic and amorphous nature with less defects. The FT-IR, BET, TGA, and Raman spectrum illustrated that most of the compounds disappeared or degraded into carbon when C-600 was activated by CO_2 at high temperatures. The gel polymer electrolyte was prepared from PVA and KOH (PVA-KOH) and used in all-solid-state SCs, while the symmetric electrodes were based on the physically activated carbon (C-850). An approximately rectangular CV and triangle shape GCD curves illustrated the EDLC of the assembled SCs. Specific capacitance values of 138.12 F g^{-1} from CV and 88.4 F g^{-1} from GCD curves were calculated. Further, an energy density of 9.6 Wh kg^{-1} with a power density of 87.86 W kg^{-1} was achieved. The values obtained for the R_S and R_{CT} were 0.54 and 17.86 ohms, respectively, showing the low ohmic electrolyte resistance/internal resistance of the electrode and charge-transfer resistance. The phase angle value at the low frequency region was 76.6° for C-850 electrodes, which portrayed the nearly capacitive behavior of the cell that was closer to the ideal capacitive behavior (90°). Though the C-850 electrode did not show very excellent electrochemical performance in terms of specific capacitance and energy density, we are highly encouraged by this strategy for the preparation of physically activated carbons from various

https://doi.org/10.1021/acsomega.3c01065
ACS Omega 2023, 8, 21653−21663

biomass precursors due to its cost-effectiveness and environmental friendliness. More detailed studies at various conditions to realize their in-depth performances in energy storage devices should be performed in the future.

■ ASSOCIATED CONTENT

Supporting Information

The Supporting Information is available free of charge at https://pubs.acs.org/doi/10.1021/acsomega.3c01065.

XPS spectra for C-600, E_{ESR} from charge−discharge curves, and comparison of various activated carbons and their supercapacitor performances (PDF)

■ AUTHOR INFORMATION

Corresponding Author

Mohammed Ashraf Gondal − *Laser Research Group, Physics Department and IRC-Hydrogen and Energy Storage, King Fahd University of Petroleum & Minerals, KFUPM, Dhahran 31261, Saudi Arabia; K.A.CARE Energy Research & Innovation Center (ERIC), King Fahd University of Petroleum & Minerals (KFUPM), Dhahran 31261, Saudi Arabia;* orcid.org/0000-0001-9570-4569; Email: magondal1@gmail.com

Authors

Aziz Ahmad − *Interdisciplinary Research Center for Hydrogen and Energy Storage (IRC-HES), King Fahd University of Petroleum & Minerals, KFUPM, Dhahran 31261, Saudi Arabia*

Muhammad Hassan − *Laser Research Group, Physics Department and IRC-Hydrogen and Energy Storage, King Fahd University of Petroleum & Minerals, KFUPM, Dhahran 31261, Saudi Arabia*

Rashid Iqbal − *College of Physics and Optoelectronic Engineering, Shenzhen University, Shenzhen, Guangdong 518060, China;* orcid.org/0000-0003-2953-6725

Sami Ullah − *K.A.CARE Energy Research & Innovation Center (ERIC), King Fahd University of Petroleum & Minerals (KFUPM), Dhahran 31261, Saudi Arabia*

Atif Saeed Alzahrani − *Interdisciplinary Research Center for Hydrogen and Energy Storage (IRC-HES), King Fahd University of Petroleum & Minerals, KFUPM, Dhahran 31261, Saudi Arabia*

Waqar Ali Memon − *Chinese Academy of Sciences, National Center for Nanoscience and Technology, Beijing 100190, China*

Fazal Mabood − *Institute of Chemical Sciences, University of Swat, Charbagh, KP 19120, Pakistan*

Saad Melhi − *Department of Chemistry, College of Science, University of Bisha, Bisha 61922, Saudi Arabia*

Complete contact information is available at: https://pubs.acs.org/10.1021/acsomega.3c01065

Notes

The authors declare no competing financial interest.

■ ACKNOWLEDGMENTS

This work was supported by the King Fahd University of Petroleum & Minerals, KFUPM Box 5040 Dahran 31261, Saudi Arabia.

■ REFERENCES

(1) Lu, X.; Yu, M.; Wang, G.; Tong, Y.; Li, Y. Flexible solid-state supercapacitors: design, fabrication and applications. *Energy Environ. Sci.* **2014**, *7*, 2160−2181.

(2) Yi, H.; Nakabayashi, K.; Yoon, S.-H.; Miyawaki, J. Study on the applicability of pressurized physically activated carbon as an adsorbent in adsorption heat pumps. *RSC Adv.* **2022**, *12*, 2558−2563.

(3) Ding, Y.; Qi, J.; Hou, R.; Liu, B.; Yao, S.; Lang, J.; Chen, J.; Yang, B. Preparation of High-Performance Hierarchical Porous Activated Carbon via a Multistep Physical Activation Method for Supercapacitors. *Energy Fuels* **2022**, *36*, 5456−5464.

(4) Lin, B.; Wang, Y. Inconsistency of economic growth and electricity consumption in China: A panel VAR approach. *J. Cleaner Prod.* **2019**, *229*, 144−156.

(5) Majumdar, A. A new industrial revolution for a sustainable energy future. *MRS Bull.* **2013**, *38*, 947−954.

(6) Rolison, D. R.; Nazar, L. F. Electrochemical energy storage to power the 21st century. *MRS Bull.* **2011**, *36*, 486−493.

(7) Guo, Y.; Wang, K.; Hong, Y.; Wu, H.; Zhang, Q. Recent progress on pristine two-dimensional metal−organic frameworks as active components in supercapacitors. *Dalton Trans.* **2021**, *50*, 11331−11346.

(8) Aziz, M. A.; Shah, S. S.; Nayem, S. M. A.; Shaikh, M. N.; Hakeem, A. S.; Bakare, I. A. Peat soil-derived silica doped porous graphitic carbon with high yield for high-performance all-solid-state symmetric supercapacitors. *J. Energy Storage* **2022**, *50*, No. 104278.

(9) Shaheen Shah, S.; Abu Nayem, S. M.; Sultana, N.; Saleh Ahammad, A. J.; Abdul Aziz, M. Preparation of Sulfur-doped Carbon for Supercapacitor Applications: A Review. *ChemSusChem* **2022**, *15*, No. e202101282.

(10) Yaseen, M.; Khattak, M. A. K.; Humayun, M.; Usman, M.; Shah, S. S.; Bibi, S.; Hasnain, B. S. U.; Ahmad, S. M.; Khan, A.; Shah, N.; et al. A Review of Supercapacitors: Materials Design, Modification, and Applications. *Energies* **2021**, *14*, 7779.

(11) Hashmi, S. A.; Suematsu, S.; Naoi, K. All solid-state redox supercapacitors based on supramolecular 1,5-diaminoanthraquinone oligomeric electrode and polymeric electrolytes. *J. Power Sources* **2004**, *137*, 145−151.

(12) Conway, B. E. *Electrochemical Supercapacitors: Scientific Fundamentals and Technical Applications*. Kluwer Academic/Plenum Publishers, New York 1999.

(13) Kötz, R.; Carlen, M. Principles and applications of electrochemical capacitors. *Electrochim. Acta* **2000**, *45*, 2483−2498.

(14) Conway, B. E. Transition from "Supercapacitor" to "Battery" Behavior in Electrochemical Energy Storage. *J. Electrochem. Soc.* **1991**, *138*, 1539−1548.

(15) Sarangapani, S.; Tilak, B. V.; Chen, C. P. Materials for Electrochemical Capacitors: Theoretical and Experimental Constraints. *J. Electrochem. Soc.* **1996**, *143*, 3791−3799.

(16) Nishino, A. Capacitors: operating principles, current market and technical trends. *J. Power Sources* **1996**, *60*, 137−147.

(17) Xie, M.; Duan, S.; Shen, Y.; Fang, K.; Wang, Y.; Lin, M.; Guo, X. In-Situ-Grown Mg(OH)2-Derived Hybrid α-Ni(OH)2 for Highly Stable Supercapacitor. *ACS Energy Lett.* **2016**, *1*, 814−819.

(18) Xie, M.; Xu, Z.; Duan, S.; Tian, Z.; Zhang, Y.; Xiang, K.; Lin, M.; Guo, X.; Ding, W. Facile growth of homogeneous Ni(OH)2 coating on carbon nanosheets for high-performance asymmetric supercapacitor applications. *Nano Res.* **2018**, *11*, 216−224.

(19) Srinivasan, V.; Weidner, J. W. Studies on the Capacitance of Nickel Oxide Films: Effect of Heating Temperature and Electrolyte Concentration. *J. Electrochem. Soc.* **2000**, *147*, 880.

(20) Zheng, J. P.; Jow, T. R. A New Charge Storage Mechanism for Electrochemical Capacitors. *J. Electrochem. Soc.* **1995**, *142*, L6−L8.

(21) Lin, C.; Ritter, J. A.; Popov, B. N. Characterization of Sol-Gel-Derived Cobalt Oxide Xerogels as Electrochemical Capacitors. *J. Electrochem. Soc.* **1998**, *145*, 4097−4103.

(22) Dong, Y.; Liu, J.; Zhang, H.; Li, Q.; Mao, F.; Lu, A.; Wu, H.; Wang, K.; Zhang, C.; Zhang, Q. Novel isostructural iron-series-MOF calcined derivatives as positive and negative electrodes: A new

strategy to obtain matched electrodes in a supercapacitor device. *SmartMat* 2022, DOI: 10.1002/smm2.1159.
(23) Ahmad, A.; Imani, A.; Mao, L.; Iqbal, R.; Zhang, H.; Ghazi, Z. A.; Ahmad, R.; Khan, A. A.; Xie, L.; Chen, C.-M.; et al. A Bifunctional and Free-Standing Organic Composite Film with High Flexibility and Good Tensile Strength for Tribological and Electrochemical Applications. *Adv. Mater. Technol.* **2019**, *4*, 1900617.
(24) Rudge, A.; Davey, J.; Raistrick, I.; Gottesfeld, S.; Ferraris, J. P. Conducting polymers as active materials in electrochemical capacitors. *J. Power Sources* **1994**, *47*, 89−107.
(25) Rudge, A.; Raistrick, I.; Gottesfeld, S.; Ferraris, J. P. A study of the electrochemical properties of conducting polymers for application in electrochemical capacitors. *Electrochim. Acta* **1994**, *39*, 273−287.
(26) Arbizzani, C.; Mastragostino, M.; Meneghello, L. Polymer-based redox supercapacitors: A comparative study. *Electrochim. Acta* **1996**, *41*, 21−26.
(27) Arbizzani, C.; Catellani, M.; Mastragostino, M.; Mingazzini, C. N- and P-doped Polydithieno[3,4-B,3′,4′-D] thiophene: A narrow band gap polymer for redox supercapacitors. *Electrochim. Acta* **1995**, *40*, 1871−1876.
(28) Mastragostino, M.; Arbizzani, C.; Paraventi, R.; Zanelli, A. Polymer Selection and Cell Design for Electric-Vehicle Supercapacitors. *J. Electrochem. Soc.* **2000**, *147*, 407.
(29) Liu, S.; Du, C.; Zhang, Y.; Xie, M.; Chen, J.; Wan, L. Oxidative-polymerization and deoxygenation of mixed phenols to faradaic-oxygen modified mesoporous carbon and its supercapacitive performances. *J. Energy Storage* **2021**, *34*, No. 102198.
(30) Patel, K. K.; Singhal, T.; Pandey, V.; Sumangala, T. P.; Sreekanth, M. S. Evolution and recent developments of high performance electrode material for supercapacitors: A review. *J. Energy Storage* **2021**, *44*, No. 103366.
(31) Osaka, T.; Liu, X.; Nojima, M.; Momma, T. An Electrochemical Double Layer Capacitor Using an Activated Carbon Electrode with Gel Electrolyte Binder. *J. Electrochem. Soc.* **1999**, *146*, 1724−1729.
(32) Borchardt, L.; Leistenschneider, D.; Haase, J.; Dvoyashkin, M. Revising the Concept of Pore Hierarchy for Ionic Transport in Carbon Materials for Supercapacitors. *Adv. Energy Mater.* **2018**, *8*, 1800892.
(33) Xu, Y.; Lin, Z.; Zhong, X.; Huang, X.; Weiss, N. O.; Huang, Y.; Duan, X. Holey graphene frameworks for highly efficient capacitive energy storage. *Nat. Commun.* **2014**, *5*, 4554.
(34) Liu, T.; Zhang, F.; Song, Y.; Li, Y. Revitalizing carbon supercapacitor electrodes with hierarchical porous structures. *J. Mater. Chem. A* **2017**, *5*, 17705−17733.
(35) Li, Z.; Guo, D.; Liu, Y.; Wang, H.; Wang, L. Recent advances and challenges in biomass-derived porous carbon nanomaterials for supercapacitors. *Chem. Eng. J.* **2020**, *397*, No. 125418.
(36) Huang, S.; Ding, Y.; Li, Y.; Han, X.; Xing, B.; Wang, S. Nitrogen and Sulfur Co-doped Hierarchical Porous Biochar Derived from the Pyrolysis of Mantis Shrimp Shell for Supercapacitor Electrodes. *Energy Fuels* **2021**, *35*, 1557−1566.
(37) Peng, C.; Yan, X.-B.; Wang, R.-T.; Lang, J.-W.; Ou, Y.-J.; Xue, Q.-J. Promising activated carbons derived from waste tea-leaves and their application in high performance supercapacitors electrodes. *Electrochim. Acta* **2013**, *87*, 401−408.
(38) Qiu, X.; Wang, L.; Zhu, H.; Guan, Y.; Zhang, Q. Lightweight and efficient microwave absorbing materials based on walnut shell-derived nano-porous carbon. *Nanoscale* **2017**, *9*, 7408−7418.
(39) Xu, X.; Gao, J.; Tian, Q.; Zhai, X.; Liu, Y. Walnut shell derived porous carbon for a symmetric all-solid-state supercapacitor. *Appl. Surf. Sci.* **2017**, *411*, 170−176.
(40) Wang, M.; Cheng, S.; Yao, M.; Zhu, Y.; Wu, P.; Luo, H.; Yang, L.; Tang, L.; Liu, M. Synthesis of biomass-derived 3D porous graphene-like via direct solid-state transformation and its potential utilization in lithium-ion battery. *Ionics* **2018**, *24*, 1879−1886.
(41) Wang, R.; Wang, P.; Yan, X.; Lang, J.; Peng, C.; Xue, Q. Promising Porous Carbon Derived from Celtuce Leaves with Outstanding Supercapacitance and CO2 Capture Performance. *ACS Appl. Mater. Interfaces* **2012**, *4*, 5800−5806.
(42) Chen, Z.-H.; Du, X.-L.; He, J.-B.; Li, F.; Wang, Y.; Li, Y.-L.; Li, B.; Xin, S. Porous Coconut Shell Carbon Offering High Retention and Deep Lithiation of Sulfur for Lithium−Sulfur Batteries. *ACS Appl. Mater. Interfaces* **2017**, *9*, 33855−33862.
(43) Halder, G.; Khan, A. A.; Dhawane, S. Fluoride Sorption Onto a Steam-Activated Biochar Derived From Cocos nucifera Shell. *Clean: Soil, Air, Water* **2016**, *44*, 124−133.
(44) Pham, H. D.; Mahale, K.; Hoang, T. M. L.; Mundree, S. G.; Gomez-Romero, P.; Dubal, D. P. Dual Carbon Potassium-Ion Capacitors: Biomass-Derived Graphene-like Carbon Nanosheet Cathodes. *ACS Appl. Mater. Interfaces* **2020**, *12*, 48518−48525.
(45) Reddy, K. S. K.; Al Shoaibi, A.; Srinivasakannan, C. A comparison of microstructure and adsorption characteristics of activated carbons by CO2 and H3PO4 activation from date palm pits. *New Carbon Mater.* **2012**, *27*, 344−351.
(46) Lu, H.; Zhao, X. S. Biomass-derived carbon electrode materials for supercapacitors. *Sustain. Energy Fuels* **2017**, *1*, 1265−1281.
(47) Abioye, A. M.; Ani, F. N. Recent development in the production of activated carbon electrodes from agricultural waste biomass for supercapacitors: A review. *Renew. Sust. Energ. Rev.* **2015**, *52*, 1282−1293.
(48) Lua, A. C.; Yang, T. Effect of activation temperature on the textural and chemical properties of potassium hydroxide activated carbon prepared from pistachio-nut shell. *J. Colloid Interface Sci.* **2004**, *274*, 594−601.
(49) Rodríguez-Reinoso, F.; Molina-Sabio, M. Activated carbons from lignocellulosic materials by chemical and/or physical activation: an overview. *Carbon* **1992**, *30*, 1111−1118.
(50) Dawson, E. A.; Parkes, G. M. B.; Barnes, P. A.; Chinn, M. J. An investigation of the porosity of carbons prepared by constant rate activation in air. *Carbon* **2003**, *41*, 571−578.
(51) Sevilla, M.; Mokaya, R. Energy storage applications of activated carbons: supercapacitors and hydrogen storage. *Energy Environ. Sci.* **2014**, *7*, 1250−1280.
(52) Roy, C. K.; Shah, S. S.; Reaz, A. H.; Sultana, S.; Chowdhury, A.-N.; Firoz, S. H.; Zahir, M. H.; Ahmed Qasem, M. A.; Aziz, M. A. Preparation of Hierarchical Porous Activated Carbon from Banana Leaves for High-performance Supercapacitor: Effect of Type of Electrolytes on Performance. *Chem. − Asian J.* **2021**, *16*, 296−308.
(53) Wang, K.; Guo, Y.; Zhang, Q. Metal−Organic Frameworks Constructed from Iron-Series Elements for Supercapacitors. *Small Struct.* **2022**, *3*, 2100115.
(54) Wang, P.; Zakeeruddin, S. M.; Moser, J. E.; Nazeeruddin, M. K.; Sekiguchi, T.; Grätzel, M. A stable quasi-solid-state dye-sensitized solar cell with an amphiphilic ruthenium sensitizer and polymer gel electrolyte. *Nat. Mater.* **2003**, *2*, 402−407.
(55) Shah, S. S.; Cevik, E.; Aziz, M. A.; Qahtan, T. F.; Bozkurt, A.; Yamani, Z. H. Jute Sticks Derived and Commercially Available Activated Carbons for Symmetric Supercapacitors with Bio-electrolyte: A Comparative Study. *Synth. Met.* **2021**, *277*, No. 116765.
(56) Wang, K.; Wang, S.; Liu, J.; Guo, Y.; Mao, F.; Wu, H.; Zhang, Q. Fe-Based Coordination Polymers as Battery-Type Electrodes in Semi-Solid-State Battery−Supercapacitor Hybrid Devices. *ACS Appl. Mater. Interfaces* **2021**, *13*, 15315−15323.
(57) Panero, S.; Clemente, A.; Spila, E. Solid state supercapacitors using gel membranes as electrolytes. *Solid State Ionics* **1996**, *86-88*, 1285−1289.
(58) Clemente, A.; Panero, S.; Spila, E.; Scrosati, B. Solid-state, polymer-based, redox capacitors. *Solid State Ionics* **1996**, *85*, 273−277.
(59) Ge, J.; Zhu, M.; Eisner, E.; Yin, Y.; Dong, H.; Karnaushenko, D. D.; Karnaushenko, D.; Zhu, F.; Ma, L.; Schmidt, O. G. Imperceptible Supercapacitors with High Area-Specific Capacitance. *Small* **2021**, *17*, 2101704.
(60) De Silva, T.; Damery, C.; Alkhaldi, R.; Karunanithy, R.; Gallaba, D. H.; Patil, P. D.; Wasala, M.; Sivakumar, P.; Migone, A.; Talapatra, S. Carbon Nanotube Based Robust and Flexible Solid-State Supercapacitor. *ACS Appl. Mater. Interfaces* **2021**, *13*, 56004−56013.

https://doi.org/10.1021/acsomega.3c01065
ACS Omega 2023, 8, 21653−21663

(61) Subramani, K.; Sudhan, N.; Divya, R.; Sathish, M. All-solid-state asymmetric supercapacitors based on cobalt hexacyanoferrate-derived CoS and activated carbon. *RSC Adv.* **2017**, *7*, 6648−6659.
(62) Hassan, M.; Gondal, M. A.; Cevik, E.; Bozkurt, A. Synthesis of a Molybdate-Chelated Biodegradable Gel Electrolyte for High Energy Density Supercapacitors. *ACS Appl. Energy Mater.* **2022**, *5*, 6833−6846.
(63) Shah, S. S.; Alfasane, M. A.; Bakare, I. A.; Aziz, M. A.; Yamani, Z. H. Polyaniline and heteroatoms−enriched carbon derived from Pithophora polymorpha composite for high performance supercapacitor. *J. Energy Storage* **2020**, *30*, No. 101562.
(64) Ganguly, A.; Sharma, S.; Papakonstantinou, P.; Hamilton, J. Probing the Thermal Deoxygenation of Graphene Oxide Using High-Resolution In Situ X-ray-Based Spectroscopies. *J. Phys. Chem. C* **2011**, *115*, 17009−17019.
(65) Lan, G.; Qiu, Y.; Fan, J.; Wang, X.; Tang, H.; Han, W.; Liu, H.; Liu, H.; Song, S.; Li, Y. Defective graphene@diamond hybrid nanocarbon material as an effective and stable metal-free catalyst for acetylene hydrochlorination. *Chem. Commun.* **2019**, *55*, 1430−1433.
(66) Jin, Y.; Tian, K.; Wei, L.; Zhang, X.; Guo, X. Hierarchical porous microspheres of activated carbon with a high surface area from spores for electrochemical double-layer capacitors. *J. Mater. Chem. A* **2016**, *4*, 15968−15979.
(67) Paraknowitsch, J. P.; Zhang, J.; Su, D.; Thomas, A.; Antonietti, M. Ionic Liquids as Precursors for Nitrogen-Doped Graphitic Carbon. *Adv. Mater.* **2010**, *22*, 87−92.
(68) Yuan, G.; Huang, W.; Guan, K.; Li, H.; Xie, Y.; Liang, Y.; Liu, Y.; Zheng, M. A universal KOH-free strategy towards nitrogen-doped carbon nanosheets for high-rate and high-energy storage devices. *J. Mater. Chem. A* **2019**, *7*, 26469−26478.
(69) Ilyas, M.; Ahmad, A.; Saeed, M. Removal of Cr (VI) from Aqueous Solutions Using Peanut shell as Adsorbent. *J. Chem. Soc. Pak.* **2013**, *35*, 760−768.
(70) Sivachidambaram, M.; Vijaya, J. J.; Kennedy, L. J.; Jothiramalingam, R.; Al-Lohedan, H. A.; Munusamy, M. A.; Elanthamilan, E.; Merlin, J. P. Preparation and characterization of activated carbon derived from the Borassus flabellifer flower as an electrode material for supercapacitor applications. *New J. Chem.* **2017**, *41*, 3939−3949.
(71) Zhu, Z.; Hu, Y.; Jiang, H.; Li, C. A three-dimensional ordered mesoporous carbon/carbon nanotubes nanocomposites for supercapacitors. *J. Power Sources* **2014**, *246*, 402−408.
(72) Yushin, G. N.; Hoffman, E. N.; Nikitin, A.; Ye, H.; Barsoum, M. W.; Gogotsi, Y. Synthesis of nanoporous carbide-derived carbon by chlorination of titanium silicon carbide. *Carbon* **2005**, *43*, 2075−2082.
(73) Korenblit, Y.; Rose, M.; Kockrick, E.; Borchardt, L.; Kvit, A.; Kaskel, S.; Yushin, G. High-Rate Electrochemical Capacitors Based on Ordered Mesoporous Silicon Carbide-Derived Carbon. *ACS Nano* **2010**, *4*, 1337−1344.
(74) Dubal, D. P.; Holze, R. All-solid-state flexible thin film supercapacitor based on Mn3O4 stacked nanosheets with gel electrolyte. *Energy* **2013**, *51*, 407−412.
(75) Zhang, L.; Zhang, W.-B.; Chai, S.-S.; Han, X.-W.; Zhang, Q.; Bao, X.; Guo, Y.-W.; Zhang, X.-L.; Zhou, X.; Guo, S.-B.; et al. Review—Clay Mineral Materials for Electrochemical Capacitance Application. *J. Electrochem. Soc.* **2021**, *168*, No. 070558.
(76) Alhebshi, N. A.; Salah, N.; Hussain, H.; Salah, Y. N.; Yin, J. Structural and Electrochemical Properties of Physically and Chemically Activated Carbon Nanoparticles for Supercapacitors. *Nanomaterials* **2022**, *12*, 122.
(77) Farma, R.; Deraman, M.; Awitdrus, A.; Talib, I. A.; Taer, E.; Basri, N. H.; Manjunatha, J. G.; Ishak, M. M.; Dollah, B. N. M.; Hashmi, S. A. Preparation of highly porous binderless activated carbon electrodes from fibres of oil palm empty fruit bunches for application in supercapacitors. *Bioresour. Technol.* **2013**, *132*, 254−261.
(78) Liu, C.; Chen, W.; Hong, S.; Pan, M.; Jiang, M.; Wu, Q.; Mei, C. Fast Microwave Synthesis of Hierarchical Porous Carbons from Waste Palm Boosted by Activated Carbons for Supercapacitors. *Nanomaterials* **2019**, *9*, 405.
(79) Dai, S.; Xi, Y.; Hu, C.; Hu, B.; Yue, X.; Cheng, L.; Wang, G. C@KCu7S4 microstructure for solid-state supercapacitors. *RSC Adv.* **2014**, *4*, 40542−40545.
(80) Zhang, S.; Pan, N. Supercapacitors Performance Evaluation. *Adv. Energy Mater.* **2015**, *5*, 1401401.
(81) Ahmad, A.; Meng, Q.; Melhi, S.; Mao, L.; Zhang, M.; Han, B.-H.; Lu, K.; Wei, Z. A Hierarchically Porous Hypercrosslinked and Novel Quinone based Stable Organic Polymer Electrode for Lithium-Ion Batteries. *Electrochim. Acta* **2017**, *255*, 145−152.
(82) Choi, B. G.; Hong, J.; Hong, W. H.; Hammond, P. T.; Park, H. Facilitated Ion Transport in All-Solid-State Flexible Supercapacitors. *ACS Nano* **2011**, *5*, 7205−7213.
(83) Vicentini, R.; Da Silva, L. M.; Cecilio Junior, E. P.; Alves, T. A.; Nunes, W. G.; Zanin, H. How to Measure and Calculate Equivalent Series Resistance of Electric Double-Layer Capacitors. *Molecules* **2019**, *24*, 1452.

https://doi.org/10.1021/acsomega.3c01065
ACS Omega 2023, 8, 21653−21663